COMPUTING AND ALGORITHM INSIGHT
Volume 2, Issue 2, December 2024 | pp. 121-152
https://doi.org/10.63208/21018-109

OPEN ACCESS
Check for updates

DEVELOPMENT AND VALIDATION OF A NOVEL ROCK BRITTLENESS INDEX FOR PREDICTING ROCK BURSTS IN WATER-SATURATED SANDSTONES

Chen Haoran[1] ✉, Nguyen Thi Minh[1], and Wang Zixuan[2]

Department of Civil Engineering, Tsinghua University, Beijing 100084, China[1]; Faculty of Civil State Key Laboratory of Institute of Rock and Soil Mechanics, Zhejiang University, Hangzhou 310058, China[2]

ABSTRACT

The brittleness index is a critical parameter for evaluating rock bursts and catastrophic failures in deep underground mining. Accurate prediction of this index is vital for monitoring rock bursts, which pose risks to miners and structural integrity in engineering projects. This study introduces a new mathematical brittleness index, incorporating crack initiation, crack damage, and peak stress, tailored for sandstones with varying water contents. The proposed index is benchmarked against established brittleness indices (B1, B2, B3, B4) using infrared radiation (IR) characteristics, specifically the variance of infrared radiation temperature (VIRT), and advanced artificial intelligence (AI) models, including k-nearest neighbor (KNN), extreme gradient boost (XGBoost), and random forest (RF). Key findings include: (1) crack initiation, elastic modulus, crack damage, and peak stress decrease as water content increases; (2) brittleness indices B1, B3, and B4 exhibit a strong positive exponential correlation ($R^2 = 0.88$) with water content, while B2 shows a negative exponential correlation ($R^2 = 0.82$); (3) the new brittleness index demonstrates robust linear correlations with B1, B3, and B4 ($R^2 > 0.85$) but a weaker negative correlation with B2 ($R^2 = 0.61$); (4) the RF model outperforms others in predicting the brittleness index, achieving $R^2 = 0.999$, RMSE = 0.383, MSE = 0.007, and MAE = 0.002. Thus, the RF model is recommended for precise brittleness prediction. These findings provide valuable insights for developing effective brittleness indices to mitigate rock burst risks in water-influenced rock engineering projects.

Keywords: *Rock Brittleness Index, Rock Burst Prediction, Water-Saturated Sandstones, Infrared Radiation, Artificial Intelligence, Random Forest*

CORRESPONDING AUTHOR:
Chen Haoran
Department of Civil Engineering, Tsinghua University, Beijing 100084, China
contact: *chenhr@mails.tsinghua.edu.cn*

ARTICLE HISTORY
Received : May 20, 2024
Final Revised : October 15, 2024
Accepted : November 11, 2024
Published : December 30, 2024

© 2024 The Author(s) | Published by Integra Academic Press | This article is an open access article and distributed under the terms and conditions of the Creative Commons Attribution (CC BY-SA) license.

1. | INTRODUCTION

The rock brittleness index serves as a vital metric for evaluating rock bursts, which are dynamic failures prevalent in deep underground operations such as mining, tunneling, and cavern construction. As depth increases, the accumulation of strain energy in surrounding rocks heightens the risk of rock bursts, where stored energy rapidly converts to kinetic energy, triggering failure [1,2,3,4,5,6,7,8,9,10,11,12,13,14,15,16,17]. Accurate prediction of the brittleness index is essential for monitoring and mitigating these events, ensuring the safety and efficiency of deep engineering projects.

With global shallow mineral deposits nearing depletion, mining and tunneling activities are increasingly shifting to greater depths to meet resource demands [18]. This trend amplifies the frequency and severity of rock bursts, necessitating robust methods to predict rock brittleness. Existing literature highlights various brittleness indices, with Meng et al. [19] categorizing them into twelve groups based on their applications in rock mechanics. Notably, indices derived from stress–strain curve parameters, such as the ratio of peak strength to peak strain [20], the inverse relationship with elastic strain [21], or the ratio of crack initiation to peak stress [22], have been widely adopted. However, these indices often overlook factors like the rate of strength degradation [23] or the influence of environmental conditions.

Water content significantly alters rock mechanical behavior, reducing brittleness and the likelihood of rock bursts in moist conditions [6,24,25,26,27,28,29,30,31,32,33]. Studies show that increased water content, ranging from 5 to 17%, diminishes elastic modulus, strength, crack initiation, and crack damage [34]. In contrast to dry rock masses, which are more susceptible to bursts [36], wet rock environments, as observed by Ortlepp [37] and Fowkes [38], exhibit lower burst frequencies. Despite these insights, many existing brittleness indices were developed for dry conditions and fail to account for water's impact, limiting their applicability in real-world settings.

Traditional stress–strain-based indices also face challenges in field applications due to inaccuracies caused by mechanical vibrations from machinery, which can disrupt strain gauge measurements [34]. This underscores the need for alternative approaches to accurately capture rock behavior under varying conditions. Infrared radiation (IR) technology offers a promising solution by monitoring thermal changes during rock deformation, fracture, and failure [49,50,51,52,53,54,55,56,57,58]. IR indices, such as variance of infrared radiation temperature (VIRT) and average infrared radiation temperature (AIRT), provide quantitative insights into rock fracturing processes [40,42,43,44,59,60,61], with VIRT being particularly effective for early failure detection [34,62].

Despite advancements, IR and artificial intelligence (AI) techniques remain underutilized in developing brittleness indices for rocks under diverse water and loading conditions. AI methods, including random forest (RF), k-nearest neighbor (KNN), and extreme gradient boost (XGBoost), have shown promise in addressing complex rock engineering problems [63,64]. However, their application to brittleness prediction, particularly in water-saturated environments, is limited. This research gap highlights the need for a new brittleness index that leverages IR characteristics and AI to enhance rock burst prediction and prevention.

This study investigates IR characteristics in sandstone samples with varying water contents under loading conditions, proposing a novel mathematical brittleness index based on crack initiation, dilatancy stress, elastic modulus, and peak stress. The index is validated against established indices (B1, B2, B3, B4) and predicted using AI models (RF, KNN, XGBoost), with performance evaluated via metrics like R^2, RMSE, MSE, and MAE. By integrating IR and AI, this research aims to provide a robust framework for predicting rock brittleness, offering theoretical and practical advancements for early warning systems in rock engineering projects.

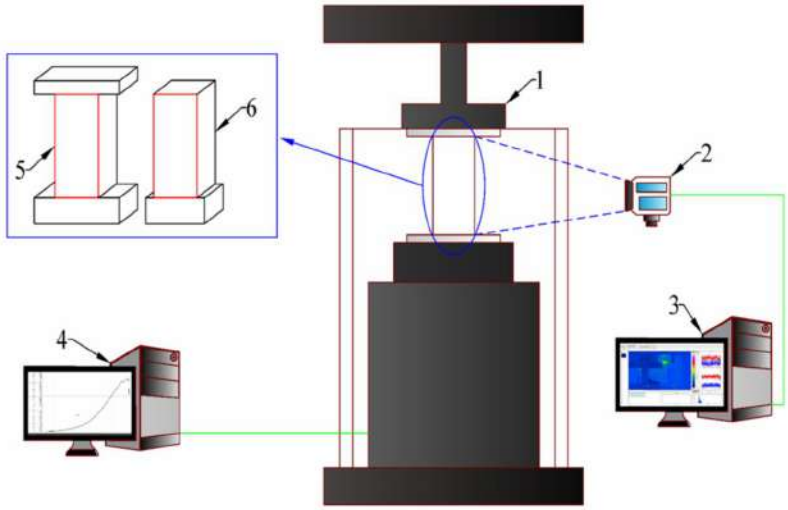
2. | MATERIALS AND METHODS

2.1. Sample Preparation

Sandstone boulders were collected from a coal mine in Shandong Province, China, and processed into rectangular specimens measuring 70 × 70 × 140 mm to maintain geometric consistency. The surfaces of these specimens were meticulously polished to ensure parallelism within a 0.2 mm tolerance. For testing purposes, the samples were categorized into four groups: K, L, M, and N. Group K samples were dried by placing them in an oven at a constant 25 °C for 48 hours, while groups L, M, and N were immersed in water for varying durations to achieve different water saturation levels. Group K samples were sealed with plastic film to prevent moisture absorption, whereas samples from the other groups remained in water until testing commenced. According to Cao et al. [50], the water saturation curve comprises three phases: a rapid increase (1–28 hours), a gradual rise (28–91 hours), and a stable phase (91–140 hours). After 118 hours, water saturation stabilized at 3.113%, indicating full saturation. The curve also shows water content at specific intervals: 0% at 0 hours, 0.991% at 5 hours, 2.136% at 20 hours, and 3.109% at 140 hours. Non-representative data points deviating from the group averages were excluded to ensure data consistency [50].

2.2. Experimental Setup

Infrared (IR) cameras (FLIR A615 model) were positioned one meter from the sandstone specimens, as depicted in Figure 1. These cameras, with a resolution of 640 × 480 pixels and a wavelength range of 7.5–14 μm, were used to capture thermal images. To mitigate end effects and heat conduction, the ends of the rock samples were wrapped in plastic before being placed in the loading machine. A consistent loading rate of 0.1 mm/min was applied, and the IR camera recorded images at a rate of 25 frames per second throughout the experiments.



1—Press machine; 2—infrared thermal imager; 3—IR data acquisition system; 4—loading control system; 5—loading sample; 6—reference sample

Figure 1. Experimental system for infrared radiation observation of sandstone under different loading rates.

2.3. Mechanical Parameters

Elasticity Modulus

The elastic modulus (E) of intact rock is a fundamental mechanical property that governs rock deformation and defines the slope of the stress–strain curve, reflecting the material's stiffness. It can be determined using three distinct methods: tangent, secant, or average modulus [65]. In this study, the average modulus was adopted, treating stress as a function of strain for computational simplicity. The elastic modulus (E) is calculated using the following equation:

$$E = \frac{Z(\varepsilon_2) - Z(\varepsilon_1)}{\varepsilon_2 - \varepsilon_1}$$

where Z(ε2) represents the peak stress, Z(ε1) denotes the stress at the onset of the elastic deformation phase, ε2 is the strain corresponding to peak stress, and (\varepsilon_1) is the strain at the start of the elastic deformation stage.

2.4. Index

2.4.1. Brittleness Index Based on Stress–Strain Curve

Stress–strain curves obtained during rock loading provide a direct and intuitive depiction of rock mechanical behavior, facilitating straightforward analysis. These curves are pivotal in developing brittleness indices, as they capture critical deformation characteristics under uniaxial or triaxial compressive conditions. Numerous brittleness indices have been formulated by analyzing the shape, structure, and behavior of these curves, offering insights into the brittle nature of rocks and their response to varying loading scenarios [8]. These indices leverage parameters such as stress, strain, and energy derived from pre- and post-peak regions of the curves to quantify brittleness and

assess the likelihood of brittle failure. A widely recognized brittleness index, B1, is calculated using the ratio of peak stress to its corresponding strain, as expressed in the following equation [21]:

$$B_1 = \frac{\sigma_p}{\varepsilon_p}$$

where σ_p is the peak stress and ε_p is the peak strain.

Wang [66] performed theoretical and preliminary analyses to establish a relationship between crack initiation stress and brittleness indices, focusing on the ratio of compressive to tensile strength. Instead of incorporating strain at crack initiation, these indices (B_2–B_4) rely solely on stress values from the stress–strain curve, leading to inconsistencies when compared to indices based on elastic modulus or energy considerations. The resulting indices exhibit discontinuous patterns and variable reliability. They are computed using the following equations:

$$B_2 = \frac{8\sigma_p}{\sigma_i}$$

$$B_3 = \frac{\sigma_i \sigma_p}{16}$$

$$B_4 = \sqrt{\frac{\sigma_i \sigma_p}{16}}$$

where σ_i represents the crack initiation stress and σ_p is the peak stress.

2.4.2. Infrared Radiation Variance (IRV)

The infrared radiation variance (IRV) is a key metric used to detect rock fractures during loading by quantifying the dispersion of infrared temperature across a rock sample's surface. As the rock undergoes deformation and damage, surface temperature variations are captured through IRV, providing insights into the fracturing process. The IRV is calculated from a sequence of IR images using the following equation:

$$IRV_x = \frac{1}{R}\frac{I}{C}\sum_{t=1}^{C}\sum_{s=1}^{R}[f_k(s,t) - AIRT_x]^2$$

where x denotes the IR image sequence frame number, s represents the row, and t represents the column of the thermograph matrix. The average infrared radiation temperature (AIRT) in the equation is defined as:

$$AIRT_x = \frac{1}{R}\frac{I}{C}\sum_{t=1}^{C}\sum_{s=1}^{R} f_x(s,t)$$

where (C) and (R) are the maximum columns and rows of the matrix, respectively.

2.5. Artificial Intelligence Techniques

2.5.1. Random Forest Algorithm

The random forest regression (RFR) algorithm, implemented via the Scikit-learn Python library, is a robust ensemble machine learning technique introduced by [66]. Widely applied in classification and regression tasks, RFR constructs multiple decision trees by randomly selecting and replacing subsets of features from the dataset, effectively handling both categorical and numerical data for predictive modeling. A notable feature of RFR is its built-in cross-validation, which ranks the importance of explanatory variables, revealing their correlation strength with the target variable [67]. In rock engineering, RFR is extensively used for applications such as predicting ground movement, assessing rock pillar stability, and evaluating landslide risks [13,48,68,69,70].

The RFR framework integrates two core components: the decision tree (DT) method and the bagging technique. Decision trees are adaptable for both classification and regression, with their application determined by the dataset's properties. The DT method partitions the feature space into smaller regions, iteratively splitting until a predefined stopping criterion is met [66]. A decision tree comprises internal nodes, which guide decision-making to subsequent nodes, and terminal (leaf) nodes, which represent final outputs that cannot be further divided. While decision trees are effective in geotechnical applications, RFR enhances predictive accuracy and robustness by aggregating multiple trees and averaging their outputs [71]. The RFR regression model is expressed as:

$$P = \frac{1}{S}\sum_{i=1}^{S} F_i(Q)$$

where Q is the input feature vector, P is the predicted outcome, S is the number of regression trees, and $F_i$represents the output of each decision tree. Figure 2 illustrates the RFR structure, where "n" denotes the total number of trees, and "Result-1" through "Result-n" represent the outputs of individual decision trees.

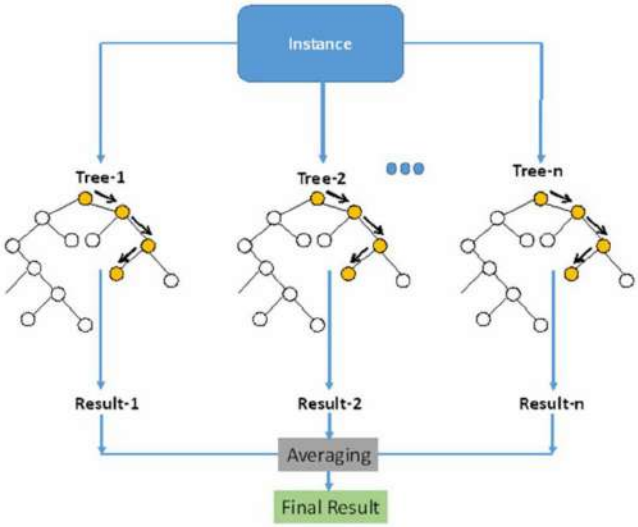


Figure 2. Basic Structure of RFR.

2.5.2. KNN

The k-nearest neighbor (KNN) algorithm is a robust machine learning technique that predicts outcomes by identifying the k-closest data points in the training dataset based on a distance metric. This method excels in scenarios with large datasets and low-dimensional feature spaces, offering simplicity and effectiveness. However, its computational cost increases in high-dimensional spaces due to the curse of dimensionality. KNN is versatile, adaptable to various tasks by modifying the distance metric or output function. For multi-label classification, KNN assigns labels based on the most frequent labels among the k-nearest neighbors. In regression tasks, it computes the average or weighted average of the k-nearest values. Additionally, KNN supports semi-supervised learning by propagating labels from labeled to unlabeled data points based on their proximity in the feature space [73].

Similar to artificial neural networks (ANN) and random forest regression (RFR), KNN is effective for both classification and regression tasks [74]. Its primary objective is to locate k samples closest to an unknown sample in the dataset using distance functions, such as Euclidean, Manhattan, or Minkowski metrics. The unknown sample is then classified or predicted by averaging the responses of these k samples [75]. The performance of KNN is highly sensitive to the choice of k, which determines the number of neighbors considered. For regression problems, the distances between points are calculated using the following equations:

$$\boldsymbol{F(a)} = \sqrt{\sum_{i=0}^{f} (\boldsymbol{k_i} - \boldsymbol{l_i})^2}$$

$$\boldsymbol{F(mb)} = \sqrt{\sum_{i=0}^{f} |\boldsymbol{k_i} - \boldsymbol{l_i}|}$$

$$\boldsymbol{F(mc)} = \left(\sqrt{\sum_{i=0}^{f} (|\boldsymbol{k_i} - \boldsymbol{l_i}|)^t} \right)^{\frac{1}{t}}$$

In these equations, $\boldsymbol{F(a)}$ denotes the Euclidean distance, $\boldsymbol{F(mb)}$ represents the Manhattan distance, and $\boldsymbol{F(mc)}$ signifies the Minkowski distance, with t indicating the order or power of the Minkowski metric. The terms $\boldsymbol{k_i}$ and $\boldsymbol{l_i}$ represent the coordinates or values of the i-th dimension for points k and l, respectively, and n is the number of dimensions.

2.5.3. Extreme Gradient Boosting

Extreme Gradient Boosting (XGBoost) is a powerful, scalable, and flexible deep learning framework based on gradient-boosted decision trees (GBDT), developed by Chen and Guestrin [76]. Renowned for its efficiency and adaptability, XGBoost

enhances predictive performance by iteratively building decision trees, where each tree corrects the errors of its predecessors. This method is particularly effective for complex datasets, making it a preferred choice for regression and classification tasks in various domains, including rock engineering. The structural components of the XGBoost model are illustrated in Figure 3, highlighting its tree-based architecture and boosting mechanism.

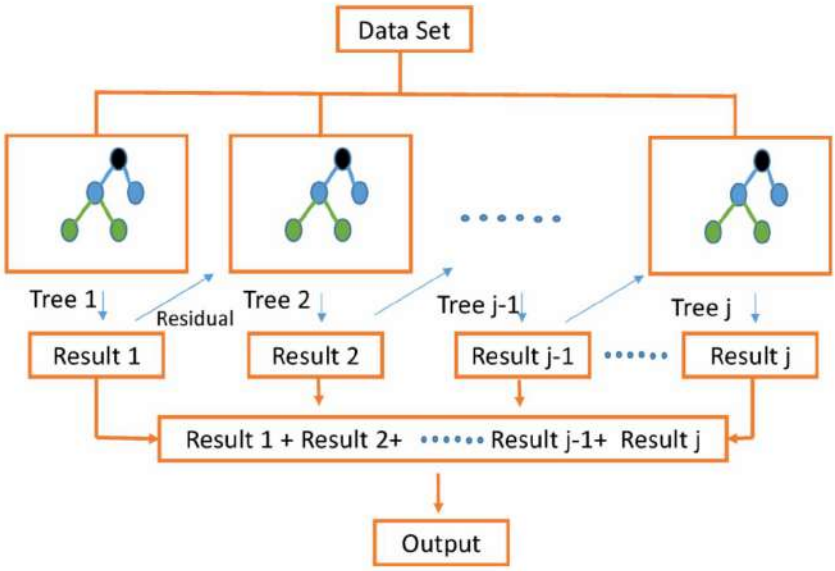


Figure 3. XGBoost model's general structure.

XGBoost is highly effective for classifying large datasets by prioritizing their complexity or the urgency required to achieve a solution, continuing until the final result is obtained. This algorithm organizes trees sequentially in a structured manner, which helps mitigate data overfitting. By arranging datasets to rank problems based on their significance, XGBoost presents associated tasks as parallel trees. Its integration into machine learning is advantageous due to its efficiency in handling large datasets and its ability to address missing data. The algorithm classifies primary issues systematically, operating on the principle that combining the optimal next model with previous ones minimizes prediction errors by the algorithm's conclusion. The machine learning strategy employed involves setting target outcomes for subsequent models to reduce errors iteratively. This top-down process continues until the aggregated results from all trees yield an accurate outcome with high efficiency [77].

3 | RESULTS AND DISCUSSION

3.1. Data Statistical Analysis

This study employs machine learning techniques with input parameters encompassing time, infrared radiation (IR), stress, and strain. Specifically, time and the variance of IR are utilized as key inputs to predict stress and strain outcomes, enabling a comprehensive analysis of rock behavior under varying conditions.

The statistical analysis results, which examine the dataset across different water content levels, are summarized in Table 1. These findings provide insights into the relationships between the input variables and the mechanical properties of the rock, facilitating accurate predictions through machine learning models.

Table 1. Statistical analysis of variables.

Parameters	Mean	Std. Deviation	Minimum	Median	Maximum
Time	473.200	273.130	0.200	473.200	946.200
IR	0.010	0.008	0.000	0.008	0.028
Strain	0.010	0.000	0.000	0.010	0.010
Stress	20.430	18.163	0.005	15.518	55.053

Figure 4 presents a heat map illustrating a strong correlation between the independent variables and the dependent variable. Additionally, it demonstrates significant inter-correlations among the independent variables themselves, indicating their effectiveness in predicting the stress–strain curve.

For this study, the dataset was divided into 70% for training and 30% for testing. To ensure uniformity across different indicators, the data were scaled and normalized to a range of (0,1). The resulting boxplot in Figure 5 visualizes the distribution of each indicator, revealing distinct variations that confirm their independence. This underscores the necessity of incorporating all input indicators to improve analytical accuracy. Notably, the training and test sets for each indicator display similar distributions, validating the random data partitioning and enhancing the reliability of the results. Figure 5a depicts the unnormalized data, highlighting dispersion in the variance of infrared radiation temperature (VIRT). Figure 5b shows the normalized data, which includes an outlier. In Figure 5c, the outlier is removed, resulting in a near-normal distribution of the normalized data.

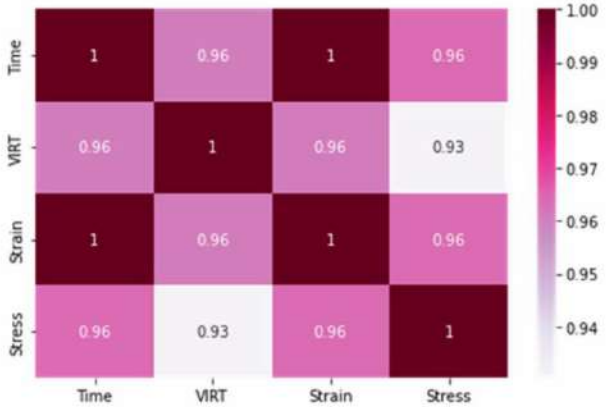


Figure 4. Heat map of dependent and independent variable.

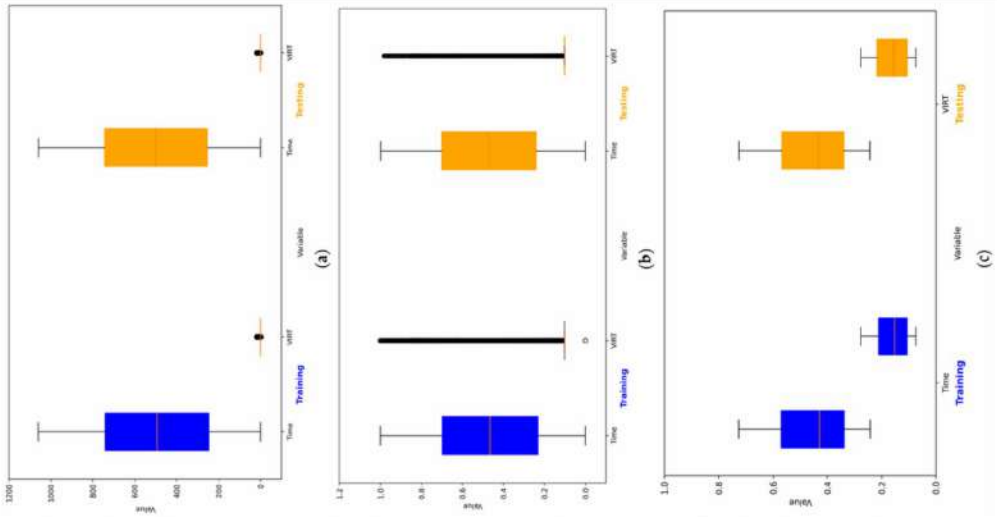


Figure 5. Box plot of input dataset: (a) the data without being normalized, (b) normalized data, (c) the normalized data without outlier.

3.2. Effect of Water on Stress–Strain

Water significantly alters the mechanical behavior of rock masses, increasing their susceptibility to damage and reducing their strength [78]. This weakening is driven by multiple factors, including the deterioration of interparticle bonds, chemical interactions, elevated pore pressure, and enhanced microcrack development. As a result, the rock's mechanical properties are compromised, making it more prone to deformation and failure. In saturated rocks under stress, the available strain energy for fracture processes diminishes, while stages of crack closure and unstable crack propagation become more pronounced. Khan et al. [79] investigated the stress–strain characteristics of rocks across varying water contents, demonstrating that peak stress, elastic modulus, crack damage stress, and crack initiation stress decrease as water content rises. This occurs due to water's lubricating effect, which exacerbates rock weakening and accelerates stress relaxation. Table 2 summarizes the key mechanical properties of sandstone under different water content levels, with findings aligning closely with those reported by Khan et al. [79].

Table 2. Mechanical properties of different water-bearing sandstone specimens.

Samples No.	Water Content (%)	E (GPa)	σ_p (MPa)	ϵ_p 10^{-2}	σ_i (MPa)	σ_d (MPa)
K-1	0.0000	10.1310	73.1210	1.2510	41.8100	63.3810
K-2	0.0000	9.8710	74.5810	0.9940	37.2300	62.2900
K-2	0.0000	9.4620	69.5520	0.8820	37.7410	57.1330
L-1	0.9710	8.7510	57.7910	1.0330	26.8200	44.1020
L-2	1.1350	8.9800	60.7720	1.1300	31.7500	42.4010
L-3	0.9910	9.3700	64.5310	1.2600	31.6000	49.6900
M-1	2.0750	7.2500	51.9230	1.1740	24.3320	38.4420
M-2	2.1360	7.9910	49.8420	1.2520	22.5500	34.9020
M-3	1.9540	7.8820	48.8930	1.1930	21.5600	33.7000
N-1	3.1090	5.8810	41.9710	1.1810	17.7910	28.1510
N-2	3.0040	5.4320	38.0320	1.2420	15.8500	28.1020
N-3	3.1130	4.8830	36.5710	1.2310	16.1800	26.3900

Note: E: elastic modulus, σ_p: peak stress; ϵ_p: peak strain, σ_i: crack initiation stress, σ_d: crack damage.

Initiation of Crack and Crack Damage Stress

To evaluate the stresses associated with crack closure, crack initiation, and dilatancy in rocks, stress–strain and stiffness–stress curves were analyzed across varying water content levels. These curves enable the precise calculation and assessment of stresses linked to each stage of crack development. Sandstone samples with different water contents were subjected to uniaxial loading, generating corresponding stress–strain and stiffness–stress curves. These responses are visually depicted in Figure 6 (stress–strain curves) and Figure 7 (stiffness–stress curves), illustrating the behavior of the samples under diverse water content conditions [79]. Point O marks the origin of the initial loading phase. As loading progresses, the curves extend to the crack closure stage, denoted as point A, where they intersect. The crack initiation point (B) is identified on the stiffness–stress curve at the location of maximum curvature, determined relative to loading time. The phase between points A and B represents the elastic deformation stage.

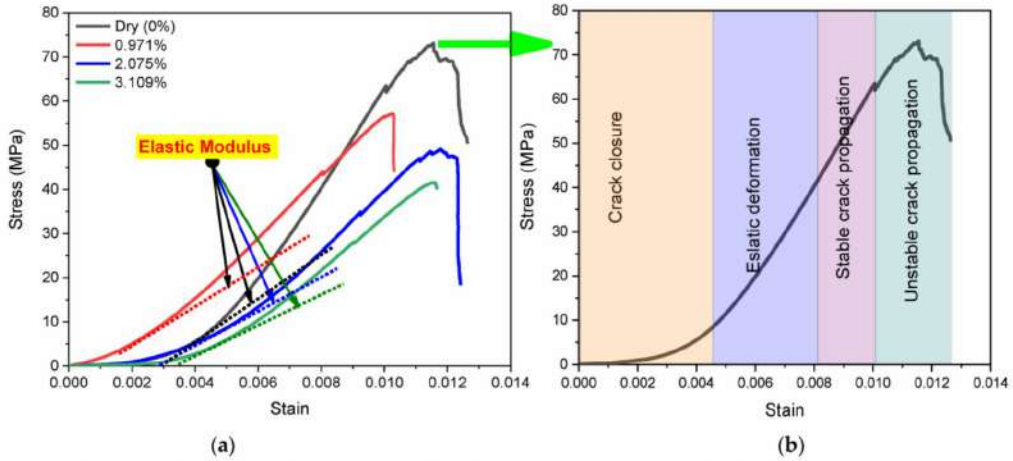


Figure 6. Stress–strain curve: (**a**) different water content; (**b**) loading stages.

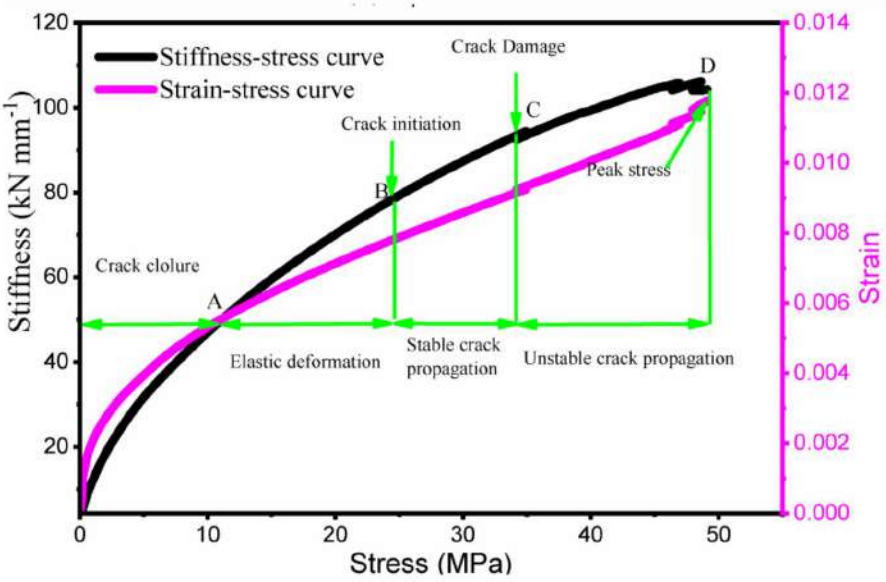


Figure 7. Stiffness–stress and stress–strain curve of sandstone.

Point C on the stiffness–stress curve marks the peak where the curve reaches its maximum value. At this juncture, a sharp drop occurs, signaling the dilatancy point, with the corresponding stress level defined as the dilatancy stress. The segment from point B to point C corresponds to the stage of progressive crack growth. As loading persists, the curve advances to point D, which indicates the maximum stress the sample can endure before failure occurs.

During the CD stage, cracks continue to propagate unstably, accompanied by audible sounds emanating from the sample. These sound waves result from the growth, expansion, and eventual coalescence of microcracks within the material. While macrocracks begin to form, the loaded samples remain structurally intact at this stage.

3.3. Effect of Water Content on Rock Behaviors

Water significantly influences geological hazards in rock engineering by infiltrating microcracks and pore spaces within rocks, leading to physical, chemical, and mechanical alterations that modify their internal structure [80]. Exposure to water generally reduces rock brittleness and strength compared to dry conditions, with the degree of change depending on rock type, water exposure duration, and volume [81]. Figure 8a illustrates the relationship between water content and the brittleness index B_1, showing an inversely proportional quadratic correlation with a coefficient of determination ($R^2 = 0.98$). Figure 8b depicts a positive linear correlation between B_2 and water content, indicating that as water content increases, B_2 values rise, reducing brittleness intensity when B_2 exceeds 10. Figure 8c reveals an inversely proportional quadratic correlation between B_3 and water content, with an R^2 of 0.99. Likewise, Figure 8d shows a quadratic correlation between B_4 and water content, with an R^2 of 0.98. The mathematical relationships between water content and the brittleness indices B_1, B_2, B_3, and B_4 are defined by Equations (12)–(15), respectively.

$$B1=75.85 - 23.46\,x+3.04\,x2 \quad R2=0.98$$

$$B2=14.843 - 1.264\,x \quad R2=0.84$$

$$B3=169.229 - 44.002\,x+1.972\,x2 \quad R2=0.99$$

$$B4=13.268 - 2.493\,x+0.081\,x2 \quad R2=0.98$$

where x is water content.

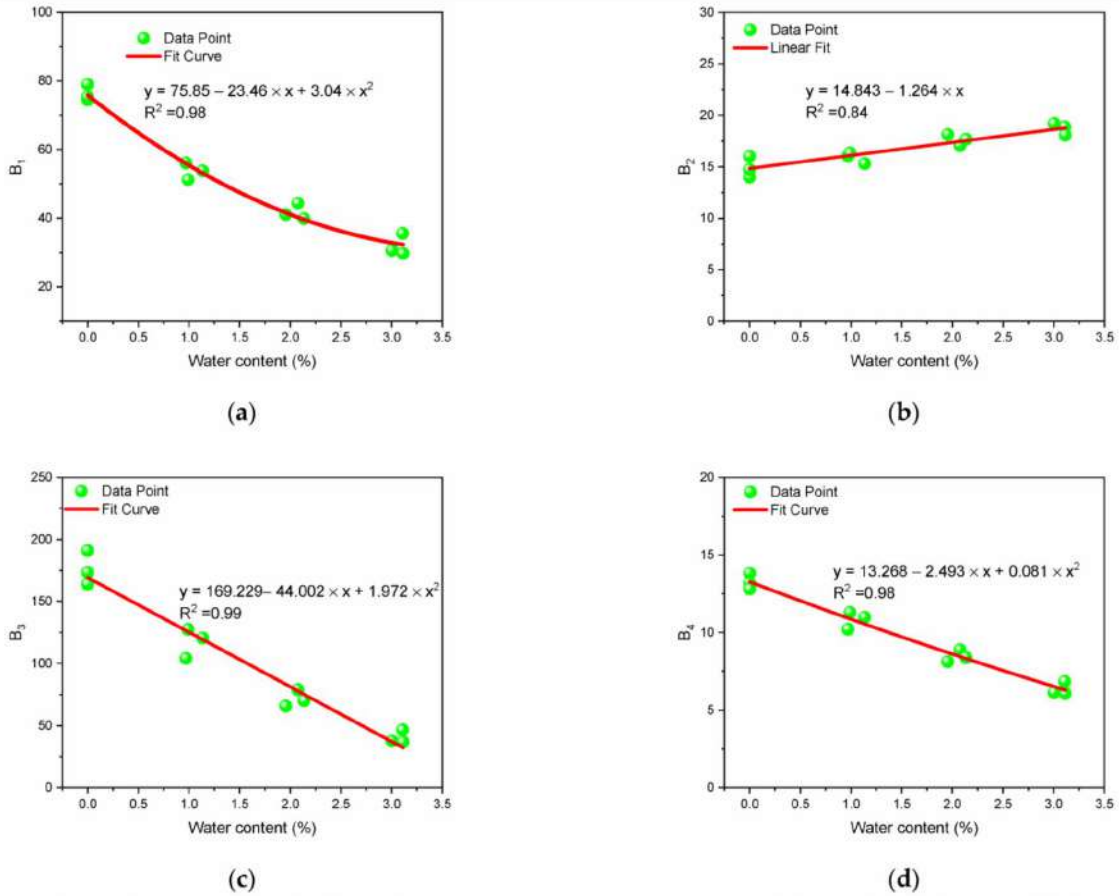


Figure 8. Relationship of different brittleness indices and water content: (**a**) B_1; (**b**) B_2; (**c**) B_3; and (**d**) B_4.

Figure 9a illustrates the relationship between elastic modulus and brittleness indices (B_1, B_2, B_3, and B_4). It indicates a positive exponential linear correlation between B1 and elastic modulus, with a coefficient of determination (R^2 = 0.86). In contrast, Figure 9b shows a negative exponential linear correlation between B2 and elastic modulus, also with an R^2 of 0.86. This inverse relationship suggests that as water content increases, the B_2 value decreases, leading to reduced brittleness intensity when B_2 exceeds 10. Figure 9c reveals a positive exponential linear correlation between B_3 and elastic modulus, with a high R^2 of 0.97. Similarly, Figure 9d demonstrates a positive exponential linear correlation between B_4 and elastic modulus, maintaining an R^2 of 0.97. The mathematical relationships between elastic modulus and the brittleness indices B_1, B_2, B_3, and B_4 under varying water contents are expressed through the following equations:

$$B_1 = e^{\frac{E}{2.252}} - 0.721E + 28.676 \quad R^2 = 0.86$$

$$B_2 = 12.882 + 5.889e^{\frac{-2(E-5.845)^2}{30.969}} \quad R^2 = 0.86$$

$$B_3 = 0.881e^{\frac{E}{1.912}} - 1.326E + 32.916 \quad R^2 = 0.97$$

$$B_4 = 0.103e^{\frac{E}{2.336}} - 0.172E + 4.389 \quad R^2 = 0.97$$

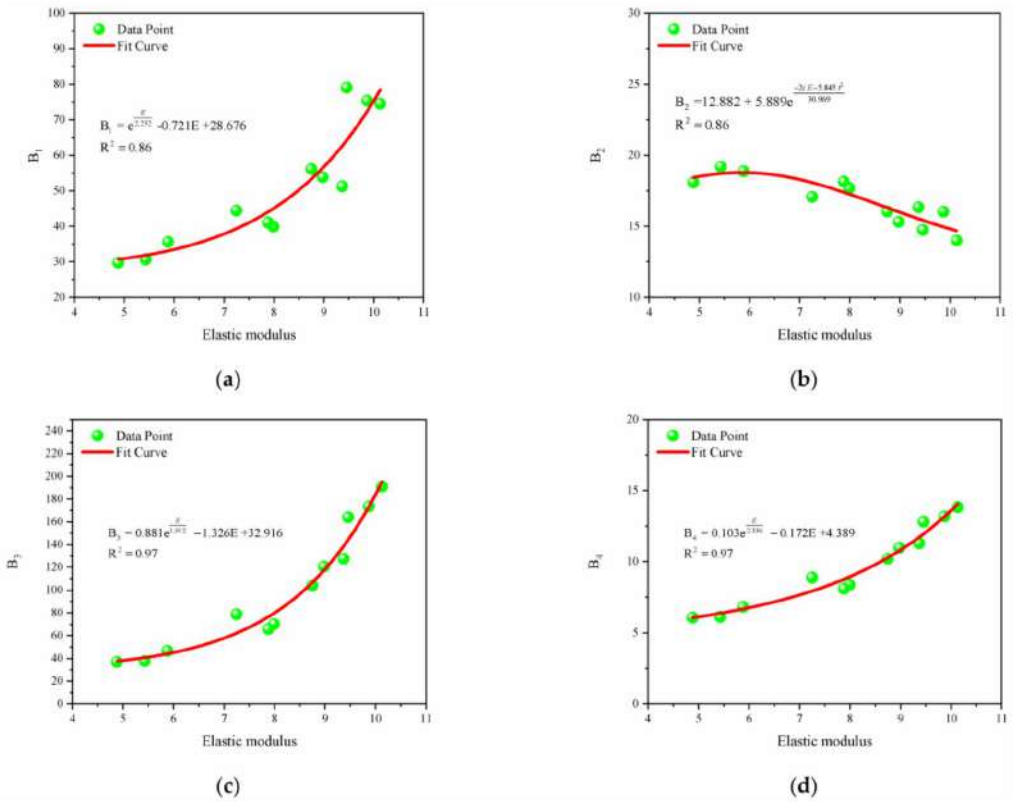
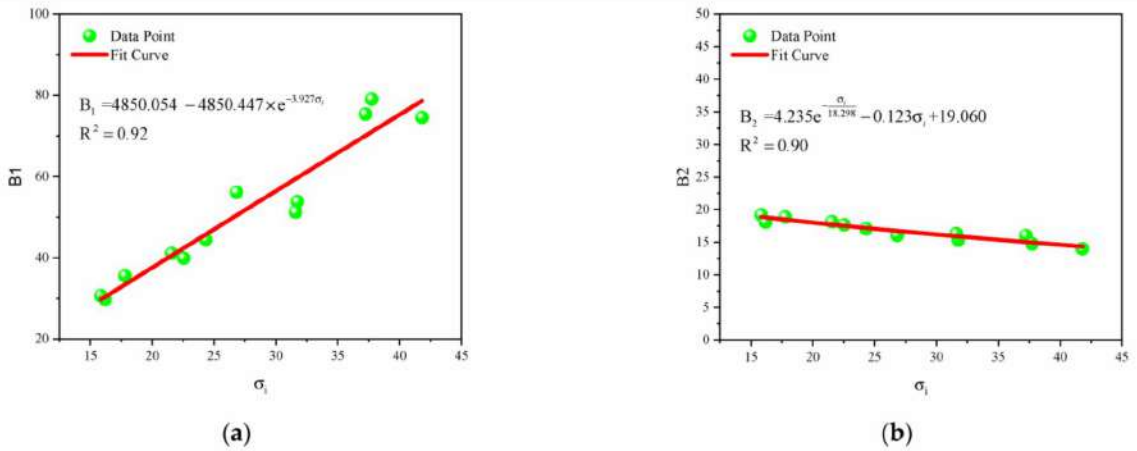


Figure 9. Relationship of different brittleness indices and elastic modulus: (**a**) B_1; (**b**) B_2; (**c**) B_3; and (**d**) B_4.

Figure 10a depicts the relationship between crack initiation stress and brittleness indices (B_1, B_2, B_3, and B_4). It demonstrates a positive exponential linear correlation between B_1 and crack initiation stress, with a coefficient of determination ($R^2 = 0.92$). Conversely, Figure 10b shows a negative exponential linear correlation between B2 and crack initiation stress, with an R^2 of 0.90. This inverse relationship indicates that as water content rises, the B_2 value increases, resulting in a decrease in brittleness intensity when B_2 exceeds 10. Figure 10c illustrates a positive exponential linear correlation between B_3 and crack initiation stress, achieving a high R^2 of 0.99. Likewise, Figure 10d reveals a positive exponential linear correlation between B_4 and crack initiation stress, also with an R^2 of 0.99. The mathematical relationships between crack initiation stress and the brittleness indices B_1, B_2, B_3, and B_4 under varying water contents are expressed through Equations (20)–(23), respectively.



(**a**) (**b**)

Figure 10. Relationship of different brittleness indices and crack initiation stress: (**a**) B_1; (**b**) B_2; (**c**) B_3; and (**d**) B_4.

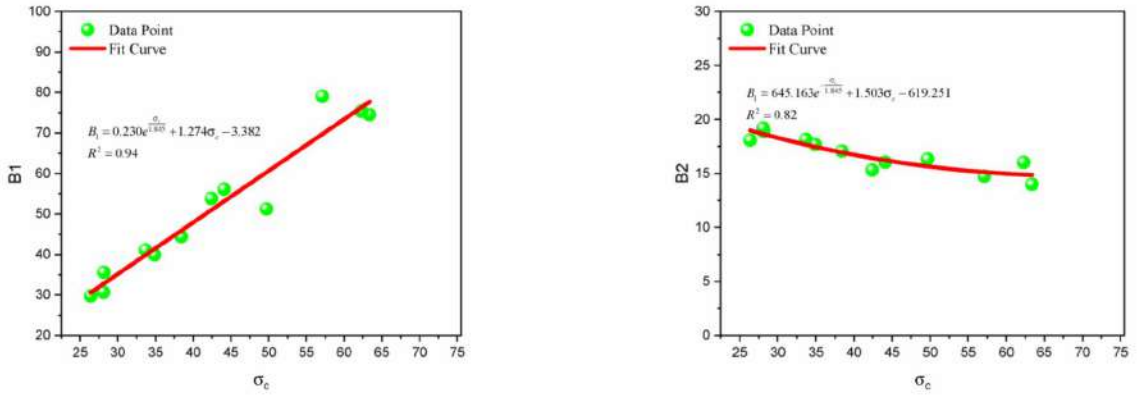
Figure 11a illustrates the relationship between crack damage stress and brittleness indices (B_1, B_2, B_3, and B_4). It indicates a positive exponential linear correlation between B_1 and crack damage stress, with a coefficient of determination ($R^2 = 0.94$). In contrast, Figure 11b shows a negative exponential linear correlation between B_2 and crack damage stress, with an R^2 of 0.82. This inverse relationship suggests that as water content increases, the B_2 value rises, leading to a reduction in brittleness intensity when B_2 exceeds 15. Figure 11c demonstrates a positive exponential linear correlation between B_3 and crack damage stress, with a high R^2 of 0.98. Similarly, Figure 11d reveals a positive exponential linear correlation between B_4 and crack damage stress, also with an R^2 of 0.98. The mathematical relationships between crack damage stress and the brittleness indices B_1, B_2, B_3, and B_4 under varying water contents are expressed through Equations (24)–(27), respectively.

$$B_1 = 0.230e^{\frac{\sigma_c}{1.845}} + 1.274\sigma_c - 3.382 \quad R^2 = 0.94$$

$$B_2 = 645.163e^{-\frac{\sigma_c}{1.845}} + 1.503\sigma_c - 619.251 \quad R^2 = 0.82$$

$$B_3 = 2.365e^{\frac{\sigma_c}{5.637}} + 4.055\sigma_c - 72.840 \quad R^2 = 0.98$$

$$B_4 = 0.852e^{\frac{\sigma_c}{1.166}} + 0.203\sigma_c - 0.252 \quad R^2 = 0.98$$



(**a**) (**b**)

Figure 11. Relationship of different brittleness indices and crack damage stress: (**a**) B_1; (**b**) B_2; (**c**) B_3; and (**d**) B_4.

The relationships between brittleness indices (B_1, B_2, B_3, and B_4) and mechanical properties such as crack initiation stress, crack damage stress, and elastic modulus exhibit strong correlations, with an average coefficient of determination (R^2) exceeding 0.82. Water content significantly influences rock behavior, reducing brittleness by approximately 41% on average and diminishing mechanical properties, including strength, elastic modulus, crack initiation, and crack damage stress. These properties display an inverse relationship with water content, indicating that rocks with higher water content are less brittle, with reduced strength and elastic modulus compared to dry conditions.

Additionally, the stages of rock loading critically affect brittleness. Rocks with higher brittleness experience shorter crack closure and stable crack propagation phases, while elastic deformation and unstable crack propagation stages become more dominant. In contrast, lower brittleness is associated with extended crack closure and stable crack propagation phases. These relationships are visually represented in Figure 5.

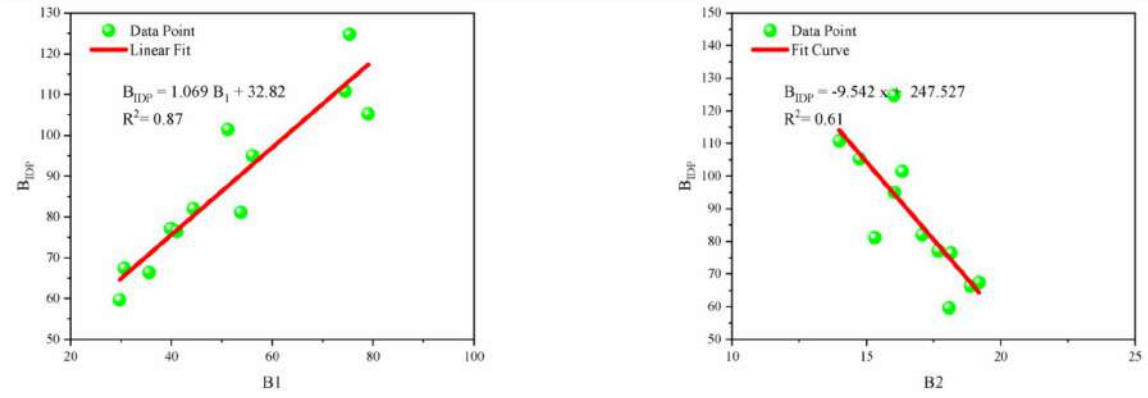
3.4. Proposed Brittleness Index under Stress–Strain Condition

Water content profoundly impacts the stress–strain behavior of rocks, influencing strain and stress levels across various phases, including crack closure, elastic deformation, and stable and unstable crack propagation. Increased water content results in higher strain and lower stress at these stages. Meng, Wong, and Zhou [19] reviewed various brittleness indices tailored to different materials and conditions. This study proposes a novel brittleness index that incorporates crack initiation stress, crack damage stress, and peak stress, specifically addressing the effects of water content. As water content rises, these stresses decrease non-proportionally, necessitating an index that accounts for their combined influence to accurately reflect rock brittleness in water-saturated conditions. This is crucial for mitigating rock burst risks in deep underground mining, where water reduces brittleness and lessens rock burst occurrences compared to dry conditions. Unlike previous indices that often overlooked water content effects, the proposed index integrates all three stress types under varying water conditions, calculated using Equation (28).

$$B_{IDP} = \frac{1}{1000\sigma_i} \times E\sigma_p\sigma_d$$

where BIDP is the brittleness index, σd is crack damage stress, σi represents crack initiation stress, and peak stress is represented by σp.

Figure 12 illustrates the relationship between the proposed brittleness index (B_IDP) and the existing brittleness indices (B_1, B_2, B_3, and B_4). The analysis reveals a strong linear correlation with B_1, B_3, and B_4, exhibiting a coefficient of determination ($R^2 = 0.87$), while a weaker negative linear correlation is observed with B_2 ($R^2 = 0.61$). The R^2 values for B_IDP with B_1, B_3, and B_4 exceed 0.80, indicating its suitability for engineering applications [82]. Table 3 provides detailed information on the brittleness intensity of the proposed B_IDP index.



(**a**) (**b**)

Figure 12. Relationship between proposed and existing brittleness index. (**a**) B_1; (**b**) B_2; (**c**) B_3; and (**d**) B_4.

Table 3. Brittleness intensity range for proposed index.

Indices	Intensity of Brittleness				
	Extreme	**High**	**Intermediate High**	**Middle**	**Low**
B_{IDP}	>100	90–100	80–90	70–80	<70

Table 4 presents the brittleness intensity of various indices compared to the proposed B_IDP index. The existing index B_1 indicates an excessively high brittleness intensity grade in water-saturated conditions, failing to accurately represent the true brittleness of rocks in this study. Similarly, indices B_2, B_3, and B_4 fall short in capturing the actual brittleness of rocks under loading across different water contents, although they perform better than B_1 in certain aspects.

The discrepancy between the actual and calculated brittleness arises from the absence of critical parameters influenced by water content in B_1, B_2, B_3, and B_4. In contrast, the proposed B_{IDP} index incorporates a comprehensive set of mechanical parameters, enabling it to accurately reflect the true brittleness conditions of rocks under varying water contents.

Table 4. Intensity comparison of proposed and existing brittleness indices.

Samples	Water Content	Previous Brittleness Indices						Proposed Brittleness Indices	
No.		**B_1**	**Grade**	**B_2**	**B_3**	**B_4**	**Grade**	**B_{IDP}**	**Grade**
K-1	0.0000	58.4960	Extremely	13.9911	191.0743	13.8230	Moderate	110.8463	Extremely
K-2	0.0000	75.3330	Extremely	16.0260	173.5407	13.1735	Moderate	124.7824	Extremely
K-2	0.0000	79.0340	Extremely	14.7430	164.0601	12.8086	Moderate	105.2891	Extremely
L-1	0.9710	56.1070	Extremely	16.0419	104.0960	10.2027	Moderate	88.4351	Moderate
L-2	1.1350	53.7790	Extremely	15.3126	120.5944	10.9815	Moderate	81.1589	Moderate
L-3	0.9910	51.2140	Extremely	16.3370	127.4487	11.2893	Moderate	99.4308	High
M-1	2.0750	44.3760	Extremely	17.0715	78.9619	8.8861	Brittle	82.0329	Moderate
M-2	2.1360	39.8720	High	17.6823	70.2461	8.3813	Brittle	77.1435	Low
M-3	1.9540	41.0840	Extremely	18.1421	65.8833	8.1169	Brittle	76.4237	Low
N-1	3.1090	35.5680	Extremely	18.8729	46.6691	6.8315	Brittle	66.4114	Low
N-2	3.0040	30.6690	Extrmely	19.1960	37.6755	6.1380	Brittle	67.4306	Low
N-3	3.1130	29.7310	Brittle	18.0821	36.9824	6.0813	Brittle	59.6483	Low

3.5. Brittleness Index Using IRV under Different Water Conditions

Figure 13 reveals the relationship between brittleness and ΔIRV. It shows that the brittleness and ΔIRV have a negative quadratic relationship with R2 = 0.90 in different water contents. The fitting function for brittleness and ΔIRV is as follows:

$$\Delta IRV = 92.58 - 1.27$$

where B is brittleness.

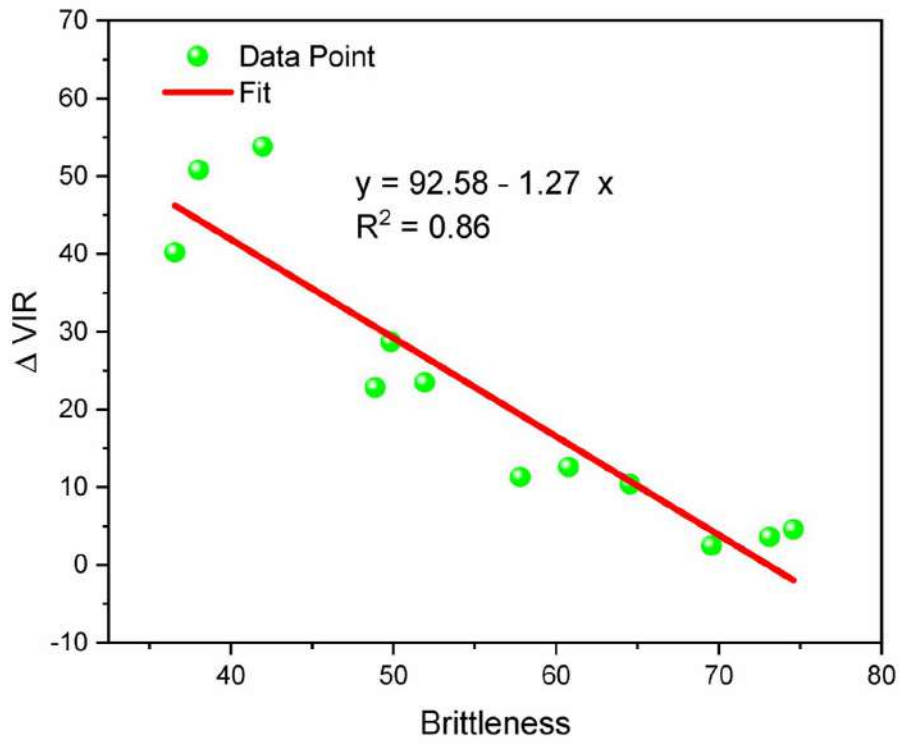


Figure 13. Relation between proposed brittleness index and VIR.

The generalized equation between brittleness and IRV is

$$\Delta IRV = \mathrm{c} - \mathrm{aB}$$

where c and a are constant

$$\mathrm{B} = \frac{-\Delta IRV}{a} + \frac{c}{a}$$

where 1/a represents the brittleness infrared radiation coefficient (BIRC) and $\frac{c}{a}$ is the brittleness constant. The rock brittleness is inversely proportional to the BIRC and directly proportional to the brittleness constant.

3.6. IRV Characteristic under Stress–Strain Curve Stages

Ma et al. [62] investigated the relationship between infrared radiation variance (IRV) and stress, as depicted in Figure 14. Their findings indicate that IRV behavior varies with water content across different fracture stages, including crack closure, elastic deformation, and stable and unstable crack propagation. In dry conditions, IRV values for these stages are 0.0018, 0.0034, 0.0035, and 0.0048, respectively, with the

lowest value observed during crack closure. In contrast, under water-saturated conditions, these values increase to 0.01265, 0.01433, 0.02223, and 0.02846, respectively. Figure 14 also highlights a strong linear correlation between stress and IRV, which is more evident in water-saturated rocks than in dry ones. The presence of water amplifies IRV, driven by higher water content. Furthermore, the study suggests that increased water content reduces rock brittleness, establishing a negative linear correlation between IRV and brittleness: higher brittleness corresponds to lower IRV, and vice versa.

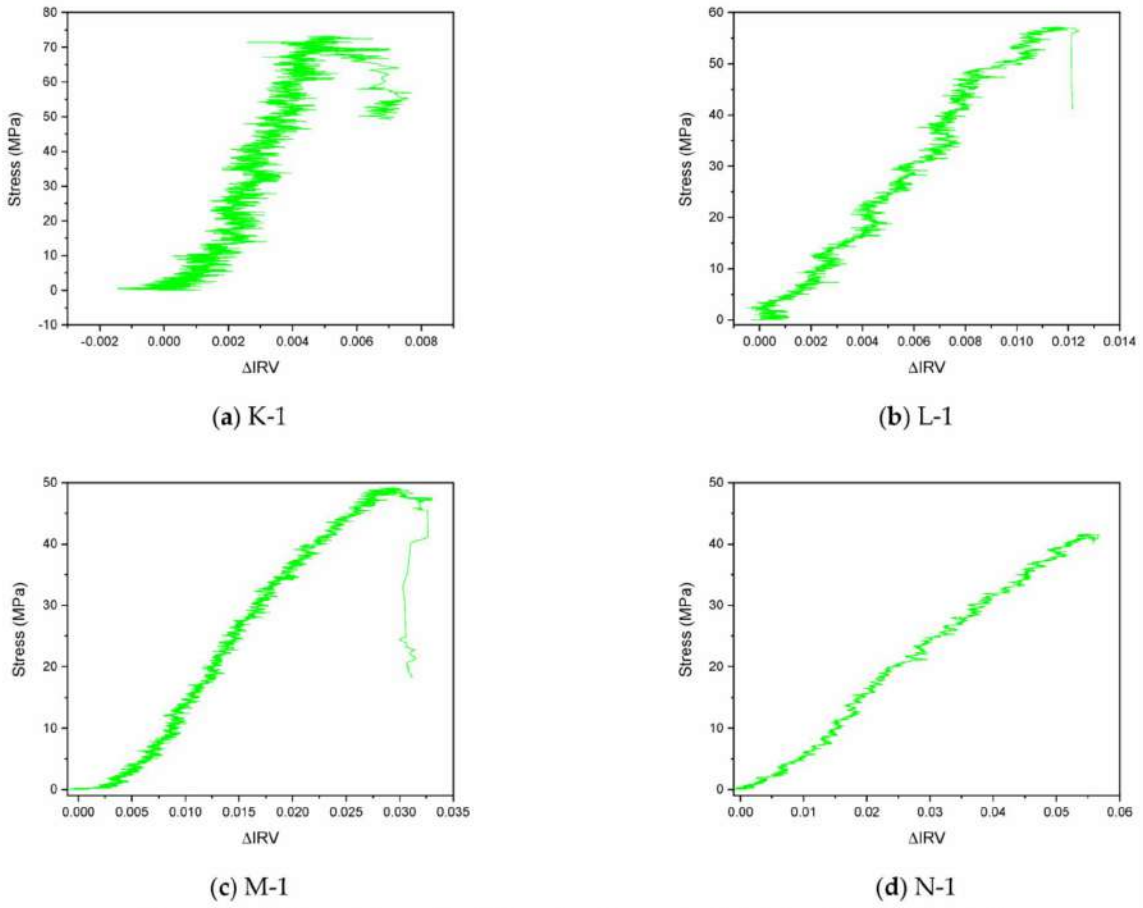


Figure 14. IRV and stress for different water content: (**a**) dry; (**b**–**d**) saturated.

Khan, Ma, Cao, Hussain, Liu, Xu, Yuan, and Gu [79] observed that stress levels decline as water content increases. They noted that while the infrared radiation variance (IRV) exhibits a positive quadratic correlation with water content, the stresses associated with fracture initiation and damage show a negative linear relationship, decreasing as water content rises. This phenomenon is attributed to the lubricating effect of water, which enhances fracture damage stress while simultaneously reducing the rate of crack initiation stress.

3.7. Prediction Models

3.7.1. Regression Models

In this research, machine learning algorithms, including k-nearest neighbors (KNN), random forest regression (RFR), and extreme gradient boosting (XGBoost), were implemented using the Scikit-Learn library in Python. The dataset was preprocessed by normalizing it to a uniform scale and then split into 70% training and 30% testing sets, as illustrated in Figure 15. During the testing phase, hyperparameter tuning was conducted to optimize each model's performance. For RFR and XGBoost, the hyperparameters "n_estimators" (indicating the number of decision trees) and "max_depth" (specifying the maximum depth of each tree) were adjusted. For KNN, the "number of neighbors" hyperparameter was fine-tuned to select the optimal number of neighbors for averaging in predictions. A grid search approach was employed to identify the best hyperparameter configurations, balancing high accuracy with minimal computational expense [83].

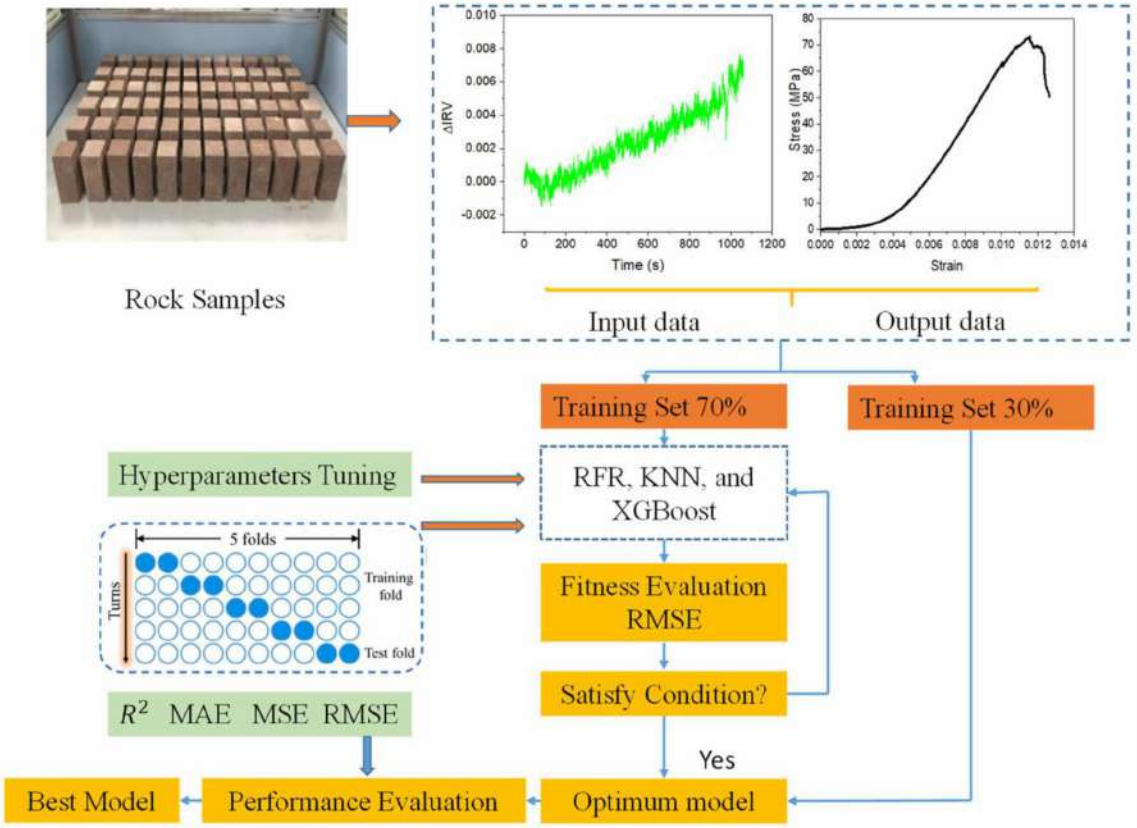


Figure 15. Flowchart of proposed model for brittleness index.

The grid search method systematically evaluates a wide range of potential values for each hyperparameter, selecting the combination that yields the best performance outcomes. For large datasets, exploring an extensive set of hyperparameter configurations can be computationally intensive, yet the priority remains on improving result reliability. To determine an effective range of hyperparameter values, each parameter is varied across different levels while holding others constant. The optimal

hyperparameter settings for each model, identified through grid search, are summarized in Table 5. Figure 16 compares the actual stress–strain data with the predicted stress–strain values generated by the model using these optimized parameters, enabling an assessment of the model's ability to accurately represent the observed stress–strain behavior.

Figure 16. Actual and predicted stress–strain curve in different water content conditions: (**a**) dry; (**b**) 0.971%; (**c**) 2.075%; (**d**) 3.109%.

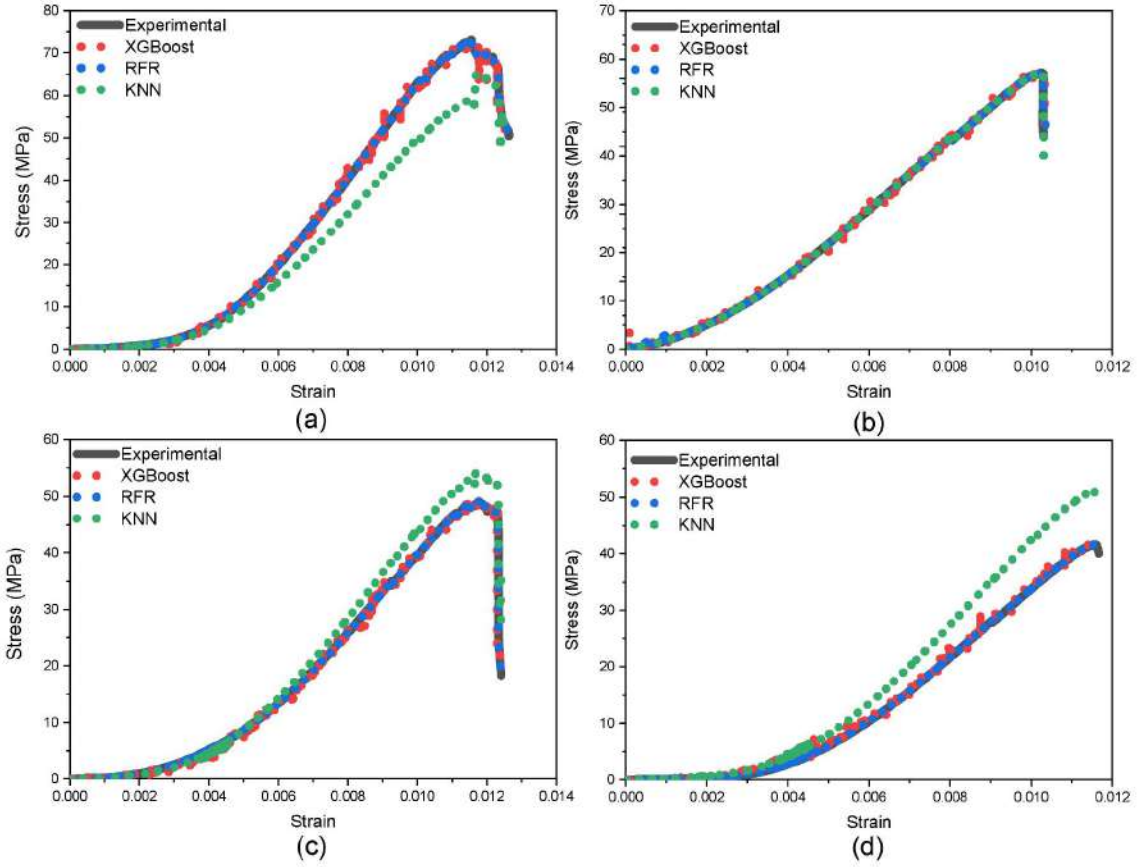


Table 5. Optimized hyperparameters of all techniques.

Output	Model	Parameters
Stress, Strain	RF	n_estimator = 30, max_depth = 13, random state = 42
	KNN	n_neighbors = 3, metric = Minkowski
	XG Boost	n_estimator = 100, reg_ lambda = 1, max_depth = 3, random state = 10

3.7.2. Performance of Models

The effectiveness of each model was evaluated using four key performance metrics: coefficient of determination (R^2), root mean square error (RMSE), mean square error (MSE), and mean absolute error (MAE). A model is considered optimal when it achieves the highest R^2 and the lowest RMSE values. Detailed performance results for each model during the training and testing phases are presented in Table 6. The models' performance, based on optimal R^2 and RMSE values, is visualized in a radar plot in Figure 17. Figure 18 compares the actual and predicted values of the proposed

brittleness index, showing that the random forest (RF) and extreme gradient boosting (XGBoost) predictions closely align with the actual values, while k-nearest neighbors (KNN) predictions are proximate but do not fully match. Among RF and XGBoost, RF demonstrates greater efficiency in predicting the brittleness index. Based on the performance metrics, the models were ranked as follows: RF > XGBoost > KNN.



Figure 17. Radar plot for comparison of XGBoost, RF, and KNN.

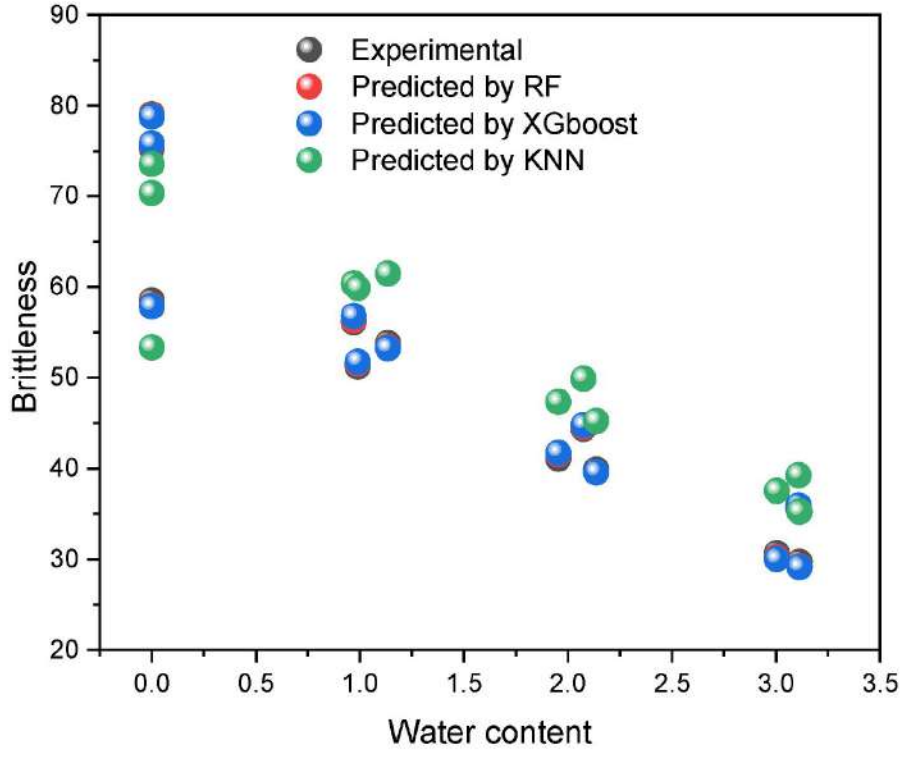


Figure 18. Actual and predicted values of brittleness for different models.

Table 6. Model efficiency during training and testing.

S.no	Models	Accuracy (Training)				Accuracy (Testing)			
		R^2	MAE	MSE	RMSE	R^2	MAE	MSE	RMSE
1	XGBoost Regressor	0.998	0.193	0.146	0.382	0.999	0.193	0.147	0.383
2	RF	0.999	0.142	0.078	0.279	0.999	0.164	0.069	0.262
3	KNN	0.853	6.195	60.961	7.807	0.853	6.201	61.017	7.811

RF dan XGBoost menunjukkan akurasi yang jauh lebih tinggi dibandingkan KNN karena beberapa alasan penting. Pertama, RF dan XGBoost merupakan metode ensemble yang memanfaatkan banyak pohon keputusan. Dengan membangun sejumlah pohon dan menggabungkan prediksinya, kedua algoritma ini mampu menangani hubungan kompleks dalam data secara lebih efektif, menghasilkan kekuatan prediktif yang lebih unggul. Sifat ensemble ini memungkinkan mereka untuk menangkap pola dan nuansa rumit dalam dataset, sehingga meningkatkan akurasi. Selain itu, RF dan XGBoost juga lebih tahan terhadap noise dan outlier jika dibandingkan dengan KNN, yang cenderung terpengaruh oleh fitur yang tidak relevan atau redundan. Mekanisme pengurangan overfitting seperti bagging pada RF dan boosting pada XGBoost juga turut berkontribusi terhadap performa mereka yang lebih stabil.

Sebaliknya, KNN mengandalkan kedekatan antar data untuk melakukan prediksi, sehingga lebih rentan terhadap noise dan fitur yang tidak relevan. Meskipun algoritma ini cukup efektif untuk dataset berukuran kecil, KNN seringkali kesulitan saat diaplikasikan pada dataset yang lebih besar atau yang memiliki banyak informasi tidak relevan. Selain itu, akurasi prediksi KNN sangat bergantung pada pemilihan nilai 'k' (jumlah tetangga terdekat), yang belum tentu optimal untuk setiap dataset, sehingga dapat menyebabkan penurunan akurasi dalam situasi tertentu. Indikator performa masing-masing model dihitung menggunakan Persamaan (32)–(35).

$$R^2 = \frac{\sum_{i=1}^{n}(k_i)^2 - \sum_{i=1}^{n}(k_i - l_i')^2}{\sum_{i=1}^{n}(k_i)^2}$$

$$RMSE = \sqrt{\frac{\sum_{i=1}^{n}(k_i - l_i')}{n}}$$

$$MSE = \frac{\sum_{i=1}^{n}(k_i - l_i')}{n}$$

$$MAE = \frac{\sum_{i=1}^{n}|(k_i - l_i')|}{n}$$

The variable k represents the actual data point value, l′ denotes the predicted value, and n indicates the total number of data points. Among the models evaluated, the

Random Forest (RF) model stands out as a robust predictor of the brittleness index. It demonstrates high efficiency by closely matching the actual values and achieving top performance across various indicators. Its ability to process large datasets while effectively mitigating overfitting highlights its reliability, although challenges such as high computational requirements and limited interpretability remain.

On the other hand, K-Nearest Neighbors (KNN) offers simplicity and performs reasonably well on smaller datasets, approximating actual values to a moderate degree. Nevertheless, its performance is constrained by its dependence on the selected k-value and vulnerability to irrelevant or noisy features. Meanwhile, the XGBoost model, based on gradient boosting, achieves commendable results and holds a strong position in predictive performance. However, it requires careful parameter tuning, has a risk of overfitting, and may not be the most suitable choice for real-time or large-scale applications. Overall, each model presents distinct advantages and limitations when applied to brittleness index prediction, making it essential to weigh these trade-offs according to the specific context of analysis.

Random Forest (RF) is highly effective in processing large datasets and numerous features, leveraging ensemble learning from multiple decision trees to reduce overfitting. Its capacity to assess feature importance also supports efficient variable selection in modeling. Despite these strengths, RF can be computationally intensive during both training and prediction, especially when using many deep trees. Furthermore, its ensemble structure can reduce interpretability and may struggle with noisy or outlier-heavy data.

K-Nearest Neighbor (KNN) is known for its simplicity and flexibility, making it ideal for smaller datasets and scenarios that do not require an explicit training phase. However, its performance heavily relies on the quality of the input features, as it can be negatively affected by redundant or irrelevant variables. The selection of the k-value is also crucial, as an inappropriate choice can lead to suboptimal results. Additionally, KNN's prediction process becomes increasingly time-consuming as the dataset grows larger.

Gradient Boosting (GBoost) delivers high accuracy by training weak learners in a sequential manner, effectively modeling complex patterns in the data. Nonetheless, its success depends on careful tuning of hyperparameters and managing the number of boosting iterations to avoid overfitting. The model's intricacy can reduce transparency and require significant computational power, which can be a limitation for real-time systems or large-scale applications.

3.8. Importance of the Research Study

Rock bursts are heavily influenced by the brittleness of elastic strain energy, with higher energy levels increasing burst intensity. Various methods, such as drilling, blasting, and water injection, have been employed to mitigate rock bursts. Among these, water injection is particularly effective, as it reduces brittleness and, consequently, rock burst severity. Water impacts sandstone's mechanical properties through several mechanisms: it modifies porosity and permeability by filling pores, potentially altering volume, density, and compressibility. Additionally, water weakens intergranular bonds and cements, particularly in rocks with clay or calcite, diminishing cohesive strength. It also acts as a lubricant, increasing pore fluid pressure, which alters stress distribution

and affects the rock's strength and deformation. Furthermore, water drives physical weathering, such as freeze–thaw cycles, causing microfractures and sandstone degradation. Chemically, water dissolves certain minerals, changing the rock's composition and mechanical behavior. Understanding these water–sandstone interactions is critical for assessing how moisture affects the rock's strength, deformability, and susceptibility to degradation [79].

Brittleness has been evaluated in various ways, with the stress–strain curve's strength-to-strain ratio at the ultimate strength point being a widely used index [23]. While effective in dry conditions, this index is less reliable in wet conditions, where loading stages reduce crack initiation and dilatancy stress, lowering brittleness and rock burst intensity. Thus, a brittleness index incorporating the ratio of dilatancy to crack initiation stress is necessary for wet conditions.

In situ stress significantly influences rock mechanics, contributing to phenomena like rock slack, bursts, and deformation, which are critical in underground engineering [84]. In situ stresses can be measured through field techniques or numerical simulations, including hydraulic fracturing, stress relief, flat jacking, borehole breakout, drilling-induced tensile fracture, acoustic emission, strain recovery, differential strain curve analysis, and geophysical methods [84]. Hydraulic fracturing and stress relief with over-coring are commonly used in borehole projects. In situ stress can destabilize rock masses around deep tunnels, acting as a load that may deform or damage the tunnel structure. Accurate measurement of regional in situ stress is essential for analyzing surrounding rock mass stability, designing underground projects, and making informed decisions [85].

However, traditional in situ stress measurement methods can produce errors due to disturbances from blasting or mechanical vibrations. To address this, infrared radiation (IR) technology has been introduced, offering non-contact, reliable results even under mechanical vibrations. Currently in a trial phase, IR technology is transitioning from laboratory testing to real-time field monitoring.

This study proposes a novel brittleness index based on the stress–strain curve, utilizing AI techniques and IR index (VIRT data) to predict stress–strain behavior. This approach achieves over 95% correlation with laboratory-derived stress–strain curves [50]. The practical applications include: (1) Predictive Analysis: Enabling engineers to forecast stress–strain behavior without extensive lab tests, improving planning and design. (2) Risk Assessment: Facilitating proactive identification of material weaknesses in mining, underground construction, or infrastructure, enhancing safety. (3) Resource Efficiency: Reducing the need for costly, time-intensive lab experiments, saving time and costs. (4) Structural Design: Supporting the design of materials and structures with tailored brittleness for optimal performance. (5) Real-time Monitoring: Providing continuous insights into material behavior when integrated into monitoring systems, critical for structural integrity [17,86,87,88,89].

Conducted on sandstone with varying water content, this study developed a tailored brittleness index. Future research will expand to other rock types (e.g., silt, granite, marble, mudstone) under diverse conditions, including varying loads, water content, high temperatures, and freeze–thaw cycles. Potential future directions include improving predictive model accuracy, exploring long-term material behavior, developing real-time monitoring systems, incorporating environmental factors into

brittleness assessments, validating methodologies, fostering interdisciplinary collaborations, and exploring new measurement techniques. These efforts aim to advance material characterization, predictive modeling, and structural safety while broadening the applicability of findings across diverse materials and conditions.

4 | CONCLUSION

This study investigated the influence of water content on sandstone brittleness under uniaxial loading, utilizing infrared radiation (IR) technology and artificial intelligence (AI) to develop a novel brittleness index, BIDP, for high-stress, water-influenced environments like deep coal mining. The findings underscore water's significant impact on rock mechanics, reducing brittleness by 41%, which lowers rock burst risks but compromises strength, increasing failure susceptibility. The proposed BIDP index, incorporating elastic modulus, crack initiation, crack damage, and peak stress, accurately reflects brittleness intensity, decreasing linearly exponentially ($R^2 > 0.90$) with water content. Compared to existing indices, BIDP shows strong linear correlations with B1, B3, and B4 ($R^2 > 0.88$) and a weaker negative correlation with B2 ($R^2 > 0.88$), highlighting its robustness. Infrared radiation variance (IRV) rates increase with water during peak stress but decline as brittleness decreases, indicating water's role in modulating IRV and rock performance. AI models—random forest (RF), XGBoost, and k-nearest neighbor (KNN)—were employed to predict BIDP, with RF demonstrating superior accuracy ($R^2 = 0.999$, RMSE = 0.383, MSE = 0.007, MAE = 0.002), making it the recommended model for brittleness prediction. These results provide a theoretical foundation for assessing rock brittleness and rock burst risks, offering practical insights for mitigating hazards in water-saturated rock engineering projects. The integration of IR and AI, coupled with the BIDP index, paves the way for innovative rock burst prevention strategies, fostering further research into advanced monitoring and management techniques for safer underground operations.

REFERENCES

1. Meng, F.; Zhou, H.; Zhang, C.; Xu, R.; Lu, J. Evaluation methodology of brittleness of rock based on post-peak stress–strain curves. *Rock Mech. Rock Eng.* 2015, 48, 1787–1805.
2. Zhao, Z.; Ali, E.; Wu, G.; Wang, X. Assessment of strain energy storage and rock brittleness indices of rockburst potential from microfabric characterizations. *Am. J. Earth Sci.* 2015, 2, 8.
3. Zhang, C.; Lu, J.; Chen, J.; Zhou, H.; Yang, F. Discussion on rock burst proneness indexes and their relation. *Rock Soil Mech.* 2017, 38, 1397–1404.
4. Zhang, L.; Cong, Y.; Meng, F.; Wang, Z.; Zhang, P.; Gao, S. Energy evolution analysis and failure criteria for rock under different stress paths. *Acta Geotech.* 2021, 16, 569–580.
5. Gong, F.; Yan, J.; Li, X.; Luo, S. A peak-strength strain energy storage index for rock burst proneness of rock materials. *Int. J. Rock Mech. Sci.* 2019, 117, 76–89.
6. Song, S.; Ren, T.; Dou, L.; Sun, J.; Yang, X.; Tan, L. Fracture features of brittle coal under uniaxial and cyclic compression loads. *Int. J. Coal Sci. Technol.* 2023, 10, 9.

7. Ali, Z.; Karakus, M.; Nguyen, G.D.; Amrouch, K. Effect of loading rate and time delay on the tangent modulus method (TMM) in coal and coal measured rocks. *Int. J. Coal Sci. Technol.* 2022, 9, 81.
8. Bai, Q.; Zhang, C.; Paul Young, R. Using true-triaxial stress path to simulate excavation-induced rock damage: A case study. *Int. J. Coal Sci. Technol.* 2022, 9, 49.
9. Chen, Y.; Zuo, J.; Liu, D.; Li, Y.; Wang, Z. Experimental and numerical study of coal-rock bimaterial composite bodies under triaxial compression. *Int. J. Coal Sci. Technol.* 2021, 8, 908–924.
10. Chi, X.; Yang, K.; Wei, Z. Breaking and mining-induced stress evolution of overlying strata in the working face of a steeply dipping coal seam. *Int. J. Coal Sci. Technol.* 2021, 8, 614–625.
11. Feng, F.; Chen, S.; Zhao, X.; Li, D.; Wang, X.; Cui, J. Effects of external dynamic disturbances and structural plane on rock fracturing around deep underground cavern. *Int. J. Coal Sci. Technol.* 2022, 9, 15.
12. He, S.; Qin, M.; Qiu, L.; Song, D.; Zhang, X. Early warning of coal dynamic disaster by precursor of AE and EMR "quiet period". *Int. J. Coal Sci. Technol.* 2022, 9, 46.
13. Huang, F.; Xiong, H.; Chen, S.; Lv, Z.; Huang, J.; Chang, Z.; Catani, F. Slope stability prediction based on a long short-term memory neural network: Comparisons with convolutional neural networks, support vector machines and random forest models. *Int. J. Coal Sci. Technol.* 2023, 10, 18.
14. Li, Y.; Mitri, H.S. Determination of mining-induced stresses using diametral rock core deformations. *Int. J. Coal Sci. Technol.* 2022, 9, 80.
15. Zhao, Y.; He, X.; Jiang, L.; Wang, Z.; Ning, J.; Sainoki, A. Influence analysis of complex crack geometric parameters on mechanical properties of soft rock. *Int. J. Coal Sci. Technol.* 2023, 10, 78.
16. Xu, L.; Fan, C.; Luo, M.; Li, S.; Han, J.; Fu, X.; Xiao, B. Elimination mechanism of coal and gas outburst based on geo-dynamic system with stress–damage–seepage interactions. *Int. J. Coal Sci. Technol.* 2023, 10, 74.
17. Soleimani, F.; Si, G.; Roshan, H.; Zhang, J. Numerical modelling of gas outburst from coal: A review from control parameters to the initiation process. *Int. J. Coal Sci. Technol.* 2023, 10, 81.
18. Munoz, H.; Taheri, A.; Chanda, E. Rock drilling performance evaluation by an energy dissipation based rock brittleness index. *Rock Mech. Rock Eng.* 2016, 49, 3343–3355.
19. Meng, F.; Wong, L.N.Y.; Zhou, H. Rock brittleness indices and their applications to different fields of rock engineering: A review. *J. Rock Mech. Geotech. Eng.* 2021, 13, 221–247.
20. Liang, L.; Liu, X.; Xiong, J.; Wu, T.; Ding, Y. New model to evaluate the Brittleness in shale formation. In *International Geophysical Conference, Qingdao, China, 17–20 April 2017*; SEG Global Meeting Abstracts; Society of Exploration Geophysicists and Chinese Petroleum Society: Houston, TX, USA, 2017; pp. 1248–1251.
21. Gong, X.; Sun, C.C. A new tablet brittleness index. *Eur. J. Pharm. Biopharm.* 2015, 93, 260–266.

22. Wang, Y.; Li, X.; Wu, Y.; Ben, Y.; Li, S.; He, J.; Zhang, B. Research on relationship between crack initiation stress level and brittleness indices for brittle rocks. *Chin. J. Rock Mech. Eng.* 2014, 33, 264–275.
23. Bishop, A. Progressive failure-with special reference to the mechanism causing it. In *Proceedings of the Geotechnical Conference Oslo 1967 on Shear Strength Properties of Natural Soils and Rocks*; Norwegian Geotechnical Institute: Oslo, Norway, 1967; pp. 142–150.
24. Baud, P.; Zhu, W.; Wong, T.F. Failure mode and weakening effect of water on sandstone. *J. Geophys. Res. Solid Earth* 2000, 105, 16371–16389.
25. Liu, X.; Yang, C.; Yu, J. The influence of moisture content on the time-dependent characteristics of rock material and its application to the construction of a tunnel portal. *Adv. Mater. Sci. Eng.* 2015, 2015, 725162.
26. Nicolas, A.; Fortin, J.; Regnet, J.; Dimanov, A.; Guéguen, Y. Brittle and semi-brittle behaviours of a carbonate rock: Influence of water and temperature. *Geophys. J. Int.* 2016, 206, 438–456.
27. Li, Y.; Yang, R.; Fang, S.; Lin, H.; Lu, S.; Zhu, Y.; Wang, M. Failure analysis and control measures of deep roadway with composite roof: A case study. *Int. J. Coal Sci. Technol.* 2022, 9, 2.
28. Liu, B.; Zhao, Y.; Zhang, C.; Zhou, J.; Li, Y.; Sun, Z. Characteristic strength and acoustic emission properties of weakly cemented sandstone at different depths under uniaxial compression. *Int. J. Coal Sci. Technol.* 2021, 8, 1288–1301.
29. Liu, T.; Lin, B.; Fu, X.; Liu, A. Mechanical criterion for coal and gas outburst: A perspective from multiphysics coupling. *Int. J. Coal Sci. Technol.* 2021, 8, 1423–1435.
30. Małkowski, P.; Niedbalski, Z.; Balarabe, T. A statistical analysis of geomechanical data and its effect on rock mass numerical modeling: A case study. *Int. J. Coal Sci. Technol.* 2021, 8, 312–323.
31. Pang, Y.; Wang, H.; Lou, J.; Chai, H. Longwall face roof disaster prediction algorithm based on data model driving. *Int. J. Coal Sci. Technol.* 2022, 9, 11.
32. Wang, G.; Ren, H.; Zhao, G.; Zhang, D.; Wen, Z.; Meng, L.; Gong, S. Research and practice of intelligent coal mine technology systems in China. *Int. J. Coal Sci. Technol.* 2022, 9, 24.
33. Wei, C.; Zhang, C.; Canbulat, I.; Song, Z.; Dai, L. A review of investigations on ground support requirements in coal burst-prone mines. *Int. J. Coal Sci. Technol.* 2022, 9, 13.
34. Khan, N.M.; Ma, L.; Cao, K.; Hussain, S.; Liu, W.; Xu, Y.; Yuan, Q.; Gu, J. Prediction of an early failure point using infrared radiation characteristics and energy evolution for sandstone with different water contents. *Bull. Eng. Geol. Environ.* 2021, 80, 6913–6936.
35. Song, Z.; Zhang, J.; Wu, S. Energy Dissipation and Fracture Mechanism of Layered Sandstones under Coupled Hydro-Mechanical Unloading. *Processes* 2023, 11, 2041.
36. Wasantha, P.L.P.; Ranjith, P.G. Water-weakening behavior of Hawkesbury sandstone in brittle regime. *Eng. Geol.* 2014, 178, 91–101.
37. Ortlepp, W.D. *Rock Fracture and Rockbursts: An Illustrative Study*; South African Institute of Mining and Metallurgy: Johannesburg, South Africa, 1997; Volume 9.

38. Fowkes, N. Rockbursts mud and plastic. In *Proceedings of the 19th International Congress on Modelling and Simulation, Modelling and Simulation Society of Australia and New Zealand, Perth, Australia, 12–16 December 2011*; pp. 12–16.
39. Gong, Q.M.; Yin, L.J.; Wu, S.Y.; Zhao, J.; Ting, Y. Rock burst and slabbing failure and its influence on TBM excavation at headrace tunnels in Jinping II hydropower station. *Eng. Geol.* 2012, 124, 98–108.
40. Wu, H.; Chen, Y.; Lv, H.; Xie, Q.; Chen, Y.; Gu, J. Stability analysis of rib pillars in highwall mining under dynamic and static loads in open-pit coal mine. *Int. J. Coal Sci. Technol.* 2022, 9, 38.
41. Wu, H.; Ju, Y.; Han, X.; Ren, Z.; Sun, Y.; Zhang, Y.; Han, T. Size effects in the uniaxial compressive properties of 3D printed models of rocks: An experimental investigation. *Int. J. Coal Sci. Technol.* 2022, 9, 83.
42. Wu, R.; Zhang, P.; Kulatilake, P.H.S.W.; Luo, H.; He, Q. Stress and deformation analysis of gob-side pre-backfill driving procedure of longwall mining: A case study. *Int. J. Coal Sci. Technol.* 2021, 8, 1351–1370.
43. Xie, J.; Ge, F.; Cui, T.; Wang, X. A virtual test and evaluation method for fully mechanized mining production system with different smart levels. *Int. J. Coal Sci. Technol.* 2022, 9, 41.
44. Xue, D.; Lu, L.; Zhou, J.; Lu, L.; Liu, Y. Cluster modeling of the short-range correlation of acoustically emitted scattering signals. *Int. J. Coal Sci. Technol.* 2021, 8, 575–589.
45. Yang, D.; Ning, Z.; Li, Y.; Lv, Z.; Qiao, Y. In situ stress measurement and analysis of the stress accumulation levels in coal mines in the northern Ordos Basin, China. *Int. J. Coal Sci. Technol.* 2021, 8, 1316–1335.
46. Yuan, Y.; Wang, S.; Wang, W.; Zhu, C. Numerical simulation of coal wall cutting and lump coal formation in a fully mechanized mining face. *Int. J. Coal Sci. Technol.* 2021, 8, 1371–1383.
47. Zhang, S.; Lu, L.; Wang, Z.; Wang, S. A physical model study of surrounding rock failure near a fault under the influence of footwall coal mining. *Int. J. Coal Sci. Technol.* 2021, 8, 626–640.
48. Zhou, J.; Lin, H.; Jin, H.; Li, S.; Yan, Z.; Huang, S. Cooperative prediction method of gas emission from mining face based on feature selection and machine learning. *Int. J. Coal Sci. Technol.* 2022, 9, 51.
49. Pappalardo, G.; Mineo, S.; Zampelli, S.P.; Cubito, A.; Calcaterra, D. InfraRed Thermography proposed for the estimation of the Cooling Rate Index in the remote survey of rock masses. *Int. J. Rock Mech. Min. Sci.* 2016, 83, 182–196.
50. Cao, K.; Ma, L.; Wu, Y.; Khan, N.; Yang, J. Using the characteristics of infrared radiation during the process of strain energy evolution in saturated rock as a precursor for violent failure. *Infrared Phys. Technol.* 2020, 109, 103406.
51. Sun, X.; Xu, H.; He, M.; Zhang, F. Experimental investigation of the occurrence of rockburst in a rock specimen through infrared thermography and acoustic emission. *Int. J. Rock Mech. Min. Sci.* 2017, 93, 9.
52. Ma, L.; Sun, H.; Zhang, Y.; Zhou, T.; Li, K.; Guo, J. Characteristics of infrared radiation of coal specimens under uniaxial loading. *Rock Mech. Rock Eng.* 2016, 49, 1567–1572.

53. Hou, L.; Ma, L.; Cao, K.; Muhammad Khan, N.; Feng, X.; Zhang, Z.; Cao, A.; Wang, D.; Wang, X. Analysis of fracture characteristics of saturated sandstone based on infrared radiation variance. *Phys. Chem. Earth Parts A/B/C* 2024, 133, 103517.
54. Cao, K.; Dong, F.; Liu, W.; Khan, N.M.; Cui, R.; Li, X.; Hussain, S.; Alarifi, S.S.; Niu, D.J.I.P. Infrared radiation denoising model of "sub-region-Gaussian kernel function" in the process of sandstone loading and fracture. *Infrared Phys. Technol.* 2023, 129, 104583.
55. Hou, L.; Cao, K.; Muhammad Khan, N.; Jahed Armaghani, D.; SAlarifi, S.; Hussain, S.; Ali, M. Precursory Analysis of Water-Bearing Rock Fracture Based on The Proportion of Dissipated Energy. *Sustainability* 2023, 15, 1769.
56. Muhammad Khan, N.; Ma, L.; Feroze, T.; Wang, D.; Cao, K.; Gao, Q.; Wang, H.; Hussain, S.; Zhang, Z.; Alarifi, S.S. Investigating average infrared radiation temperature characteristics during shear and tensile cracks in sandstone under different water contents. *Infrared Phys. Technol.* 2023, 135, 104968.
57. Cao, K.; Dong, F.; Ma, L.; Khan, N.M.; Alarifi, S.S.; Hussain, S.; Armaghani, D.J. Infrared radiation constitutive model of sandstone during loading fracture. *Infrared Phys. Technol.* 2023, 133, 104755.
58. Cao, K.; Dong, F.; Yu, Y.; Khan, N.M.; Hussain, S.; Alarifi, S.S. Infrared radiation response mechanism of sandstone during loading and fracture process. *Theor. Appl. Fract. Mech.* 2023, 126, 103974.
59. Wu, L.; Liu, S.; Wu, Y.; Wang, C. Precursors for rock fracturing and failure—Part II: IRR T-Curve abnormalities. *Int. J. Rock Mech. Min. Sci.* 2006, 43, 483–493.
60. Liu, S.; Wu, L.; Wu, Y. Infrared radiation of rock at failure. *Int. J. Rock Mech. Min. Sci.* 2006, 43, 972–979.
61. Ma, L.; Zhang, Y. An Experimental Study on Infrared Radiation Characteristics of Sandstone Samples Under Uniaxial Loading. *Rock Mech. Rock Eng.* 2019, 52, 3493–3500.
62. Ma, L.; Khan, N.M.; Cao, K.; Rehman, H.; Salman, S.; Rehman, F.U. Prediction of Sandstone Dilatancy Point in Different Water Contents Using Infrared Radiation Characteristic: Experimental and Machine Learning Approaches. *Lithosphere* 2022, 2021, 3243070.
63. Wei, Y.; Li, Z.; Kong, X.; Zhang, Z.; Cheng, F.; Zheng, X.; Wang, C. The precursory information of acoustic emission during sandstone loading based on critical slowing down theory. *J. Geophys. Eng.* 2018, 15, 2150–2158.
64. Sharma, L.K.; Singh, T.N. Regression-based models for the prediction of unconfined compressive strength of artificially structured soil. *Eng. Comput.* 2018, 34, 175–186.
65. Huang, B.; Liu, J. The effect of loading rate on the behavior of samples composed of coal and rock. *Int. J. Rock Mech. Min. Sci.* 2013, 61, 23–30.
66. Breiman, L. Random forests. *Mach. Learn.* 2001, 45, 5–32.
67. Ogunkunle, T.F.; Okoro, E.E.; Rotimi, O.J.; Igbinedion, P.; Olatunji, D.I. Artificial intelligence model for predicting geomechanical characteristics using easy-to-acquire offset logs without deploying logging tools. *Petroleum* 2022, 8, 192–203.
68. Qi, C.; Fourie, A.; Du, X.; Tang, X. Prediction of open stope hangingwall stability using random forests. *Nat. Hazards* 2018, 92, 1179–1197.

69. Zhou, J.; Li, X.; Mitri, H.S. Comparative performance of six supervised learning methods for the development of models of hard rock pillar stability prediction. *Nat. Hazards* 2015, 79, 291–316.
70. Qi, Q.; Yue, X.; Duo, X.; Xu, Z.; Li, Z. Spatial prediction of soil organic carbon in coal mining subsidence areas based on RBF neural network. *Int. J. Coal Sci. Technol.* 2023, 10, 30.
71. Khan, N.M.; Cao, K.; Yuan, Q.; Bin Mohd Hashim, M.H.; Rehman, H.; Hussain, S.; Emad, M.Z.; Ullah, B.; Shah, K.S.; Khan, S. Application of machine learning and multivariate statistics to predict uniaxial compressive strength and static Young's modulus using physical properties under different thermal conditions. *Sustainability* 2022, 14, 9901.
72. Yang, Z.; Wu, Y.; Zhou, Y.; Tang, H.; Fu, S. Assessment of Machine Learning Models for the Prediction of Rate-Dependent Compressive Strength of Rocks. *Minerals* 2022, 12, 731.
73. Wu, X.; Kumar, V.; Ross Quinlan, J.; Ghosh, J.; Yang, Q.; Motoda, H.; McLachlan, G.J.; Ng, A.; Liu, B.; Yu, P.S.; et al. Top 10 algorithms in data mining. *Knowl. Inf. Syst.* 2008, 14, 1–37.
74. Akbulut, Y.; Sengur, A.; Guo, Y.; Smarandache, F. NS-k-NN: Neutrosophic Set-Based k-Nearest Neighbors Classifier. *Symmetry* 2017, 9, 179.
75. Qian, Y.; Zhou, W.; Yan, J.; Li, W.; Han, L. Comparing Machine Learning Classifiers for Object-Based Land Cover Classification Using Very High Resolution Imagery. *Remote Sens.* 2015, 7, 153–168.
76. Chen, T.; Guestrin, C. Xgboost: A scalable tree boosting system. In *Proceedings of the 22nd ACM SIGKDD International Conference on Knowledge Discovery and Data Mining, San Francisco, CA, USA, 13–17 August 2016*; pp. 785–794.
77. Zhu, X.; Chu, J.; Wang, K.; Wu, S.; Yan, W.; Chiam, K. Prediction of rockhead using a hybrid N-XGBoost machine learning framework. *J. Rock Mech. Geotech. Eng.* 2021, 13, 1231–1245.
78. Liu, X.; Chen, H.; Liu, B.; Wang, S.; Liu, Q.; Luo, Y.; Luo, J. Experimental and numerical investigation on failure characteristics and mechanism of coal with different water contents. *Int. J. Coal Sci. Technol.* 2023, 10, 49.
79. Ma, L.; Muhammad Khan, N.; Feroze, T.; Sazid, M.; Cao, K.; Hussain, S.; Gao, Q.; Alarifi, S.S.; Wang, H. Prediction of rock loading stages using average infrared radiation temperature under shear and uniaxial loading. *Infrared Phys. Technol.* 2024, 136, 105084.
80. Zhao, Y.; Zhang, L.; Wang, W.; Tang, J.; Lin, H.; Wan, W. Transient pulse test and morphological analysis of single rock fractures. *Int. J. Rock Mech. Min. Sci.* 2017, 91, 139–154.
81. Liu, X.; Fu, Y.; Zheng, Y.; Liang, N. A review on deterioration of rock caused by water-rock interaction. *Chin. J. Undergr. Space Eng.* 2012, 8, 77–82.
82. Cao, K.; Ma, L.; Zhang, D.; Lai, X.; Zhang, Z.; Khan, N.M. An experimental study of infrared radiation characteristics of sandstone in dilatancy process. *Int. J. Rock Mech. Min. Sci.* 2020, 136, 104503.
83. Liashchynskyi, P.; Liashchynskyi, P. Grid search, random search, genetic algorithm: A big comparison for NAS. *arXiv* 2019, arXiv:1912.06059.

84. Yang, H.Q.; Zeng, Y.Y.; Lan, Y.F.; Zhou, X.P. Analysis of the excavation damaged zone around a tunnel accounting for geostress and unloading. *Int. J. Rock Mech. Min. Sci.* 2014, 69, 59–66.
85. Chai, C.; Ling, S.; Wu, X.; Hu, T.; Sun, D. Characteristics of the In Situ Stress Field and Engineering Effect along the Lijiang to Shangri-La Railway on the Southeastern Tibetan Plateau, China. *Adv. Civ. Eng.* 2021, 2021, 6652790.
86. Deng, D.; Wang, H.; Xie, L.; Wang, Z.; Song, J. Experimental study on the interrelation of multiple mechanical parameters in overburden rock caving process during coal mining in longwall panel. *Int. J. Coal Sci. Technol.* 2023, 10, 47.
87. Tan, Y.; Ma, Q.; Liu, X.; Liu, X.; Elsworth, D.; Qian, R.; Shang, J. Study on the disaster caused by the linkage failure of the residual coal pillar and rock stratum during multiple coal seam mining: Mechanism of progressive and dynamic failure. *Int. J. Coal Sci. Technol.* 2023, 10, 45.
88. Leśniak, G.; Brunner, D.J.; Topór, T.; Słota-Valim, M.; Cicha-Szot, R.; Jura, B.; Skiba, J.; Przystolik, A.; Lyddall, B.; Plonka, G. Correction to: Application of long-reach directional drilling boreholes for gas drainage of adjacent seams in coal mines with severe geological conditions. *Int. J. Coal Sci. Technol.* 2023, 10, 39.
89. Luo, J.; Li, Y.; Meng, X.; Guo, Q.; Zhao, G. Influence of coupling mechanism of loose layer and fault on multi-physical fields in mining areas. *Int. J. Coal Sci. Technol.* 2023, 10, 86.